Electronic and optical properties of the monolayer group-IV monochalcogenides MX (M = Ge, Sn; X = S, Se, Te)

Lei Xu,[1] Ming Yang,[2] Shi Jie Wang,[2] and Yuan Ping Feng[1,3,*]

[1]*Department of Physics, National University of Singapore, Singapore 117542, Singapore*
[2]*Institute of Materials Research and Engineering, A*STAR, 2 Fusionopolis Way, Innovis, Singapore 138634, Singapore*
[3]*Centre for Advanced 2D Materials and Graphene Research Centre, National University of Singapore, Singapore 117546, Singapore*

(Received 17 March 2017; revised manuscript received 2 June 2017; published 27 June 2017)

By using density-functional theory and many-body perturbation theory based first-principles calculations, we have systematically investigated the electronic and optical properties of monolayer group-IV monochalcogenides MX (M = Ge, Sn; X = S, Se, Te). All MX monolayers are predicted to be indirect gap semiconductors, except the GeSe monolayer, which has a direct gap of 1.66 eV. The carrier mobilities of MX monolayers are estimated to be on the order of 10^3 to 10^5 cm^2 V^{-1} s^{-1}, which is comparable to, and in some cases higher than, that of phosphorene using a phonon-limited scattering model. Moreover, the optical spectra of MX monolayers obtained from GW-Bethe-Salpeter equation calculations are highly orientation dependent, especially for the GeS monolayer, suggesting their potential application as a linear polarizing filter. Our results reveal that the GeSe monolayer is an attractive candidate for optoelectronic applications as it is a semiconductor with a direct band gap, a relatively high carrier mobility, and an onset optical absorption energy in the visible light range. Finally, based on an effective-mass model with nonlocal Coulomb interaction included, we find that the excitonic effects of the GeSe monolayer can be effectively tuned by the presence of dielectric substrates. Our studies provide an improved understanding of electronic, optical, and excitonic properties of group-IV monochalcogenides monolayers and might shed light on their potential electronic and optoelectronic applications.

DOI: 10.1103/PhysRevB.95.235434

I. INTRODUCTION

The successful isolation of graphene triggered enormous interest in two-dimensional (2D) materials. Besides graphene, a large number of 2D materials such as monolayer boron nitride (BN), transition-metal dichalcogenides (TMDs), and phosphorene have been extensively investigated [1–5]. Due to the reduced dimensionality, these 2D materials have unique electronic and optical properties which are not found in their parent bulk materials and are expected to bring novel applications in electronic, spintronic, and optoelectronic devices [1,5–8]. A recent addition to the 2D material family is group-VI monochalcogenides, MX (M = Ge, Sn; X = S, Se, Te). Similar to black phosphorus, bulk group-VI monochalcogenides adopt the orthorhombic crystal structure, with the *Pnma* space group, in which MX layers are held together by the van der Waals force [9,10]. It is noted that few-layer MXs have been experimentally realized [11–13] and MX monolayers (MLs) have been predicted to be dynamically stable and can be mechanically exfoliated from bulk MX phase [14,15].

Compared to other 2D materials, MX MLs are expected to exhibit certain appealing properties which can be explored for technological applications. For example, MX MLs are predicted to have superior mechanical flexibility, high optical absorption, and a high thermoelectric coefficient [11–13]. In addition, their phosphorene like structures are expected to give rise to anisotropy in carrier mobility, thermal conductivity, and optical absorption. However, in contrast to phosphorene, the MX MLs are binary compounds, consisting of two types of elements from columns IVA and VIA of the periodic table, respectively. As a result, a direction-dependent spin-orbit splitting occurs in the band structure of MX MLs due to the broken inversion symmetry [9,16]. Furthermore, recent theoretical work has predicted the coexistence of ferroelectricity and ferroelasticity in MX MLs [17], suggesting potential application of monolayer MXs in nonvolatile memory. First-principles calculations also predicted that MX MLs are more stable and more oxidation resistant than phosphorene [18], which is important for practical applications as phosphorene suffers from poor structural stability and vulnerability to oxidation when exposed in air.

Certain properties of some MX MLs have been investigated in a number of theoretical studies [9,19–21]. However, a systematic study of monolayer group-IV monochalcogenides MX is still lacking. In view of the interesting properties and broad potential applications, it is important to systematically investigate both experimentally and theoretically the properties of this group of 2D materials. Here, we present results of our systematic study of the electronic and optical properties of monolayer group-IV monochalcogenides MX using first-principles calculations based on density-functional theory and many-body perturbation theory. Our results show that all MX MLs are semiconductors with indirect band gaps, except the GeSe monolayer. Based on a phonon-limited scattering model, we predict high carrier mobilities for MX MLs. In addition, the onset absorption energies of MX MLs are found to lie in the near-infrared and visible frequency range. These extraordinary properties suggest that MX MLs are promising materials for electronic and optoelectronic applications. Moreover, by employing the effective-mass model which takes the nonlocal Coulomb interaction into consideration, we study explicitly the exciton properties and the impact of a dielectric substrate on

*Author to whom correspondence should be addressed: phyfyp@nus.edu.sg

 ©2017 American Physical Society

the excitonic effects, which provide useful guidance to tailor the excitonic effects by substrate engineering.

II. COMPUTATIONAL DETAILS

Our first-principles calculations are performed using the Vienna Ab initio Simulation Package (VASP) [22] with generalized gradient approximation (GGA) of the Perdew-Burke-Ernzerhof (PBE) functional [23]. The ion-electron interaction is treated with the projector augmented-wave (PAW) method [24]. Electron wave function is expanded on a plane-wave basis set with a cutoff energy of 500 eV. Brillouin zone integrations are performed with a Γ-centered $10 \times 12 \times 1$ grid following the scheme proposed by Monkhorst-Pack [25] throughout the whole calculations. In order to avoid spurious interaction between repeated slabs, a vacuum layer of 20 Å is imposed along the direction normal to the surfaces of MX MLs. Structure relaxation is carried out using the conjugate-gradient algorithm until the total energy converges to 10^{-6} eV and the Hellmann-Feynman force on each atom is less than 0.003 eV/Å. As it is well known that DFT-GGA calculations underestimate band gaps of semiconductors, we employ the more accurate GW approach to calculate the electronic band structures of MX MLs. In the one-shot G_0W_0 calculation, the quasiparticle energies are obtained from the DFT-GGA wave functions. At least 180 conduction bands are included, and the energy cutoff for the response function is set to be 150 eV. Since GW calculation can be performed only on a uniform mesh grid, we use the maximally localized Wannier function [26] as implemented in the WANNIER90 package [27] to interpolate the quasiparticle band structure, where p orbitals of group-IV and chalcogen atoms are chosen for the initial projections. In order to obtain the optical spectra and the corresponding exciton binding energies, the BSE calculations are carried out on top of the one-shot G_0W_0 with the Tamm-Dancoff approximation [28], which performs very well for semiconductors. The six highest valence bands and the six lowest conduction bands are included as the basis for excitonic eigenstates.

III. QUASIPARTICLE BAND STRUCTURES OF MX MONOLAYERS

The MX MLs have the same structure as phosphorene and can be obtained from the latter by replacing phosphorus atoms alternatively with a group-IV atom and a chalcogen atom. The atomic structure of monolayer MX is shown in Fig. 1, along with the corresponding first Brillouin zone in which the high-symmetry points are indicated. For convenience of discussion, we choose the x axis to be along the armchair direction and the y axis to be along the zigzag direction. The lattice parameters of the fully relaxed structures are given in Table I, which are in good agreement with results of previous studies [9,19,20].

To investigate the electronic properties of MX MLs, we calculated their quasiparticle band structures by the one-shot G_0W_0 approximation and the Wannier interpolation method and present the results in Fig 2. First of all, it is found that most of MX MLs studied here possess an indirect band gap where the valence-band maximum (VBM) lies along the

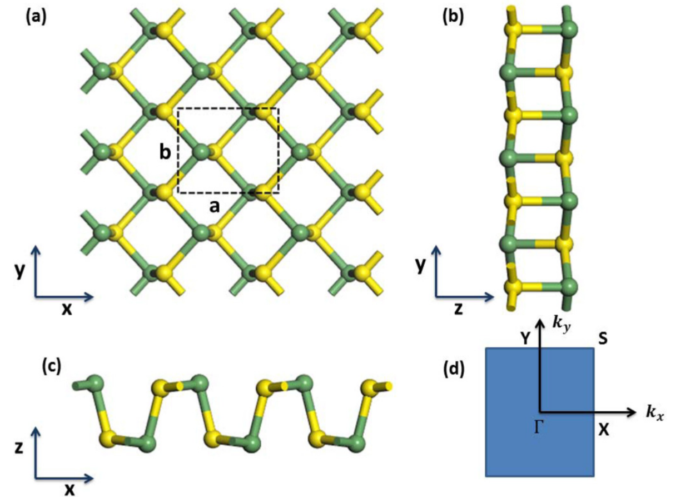

FIG. 1. (a) Top view, (b) side view along the x direction, and (c) side view along the y direction of the MX monolayer structure. Group-IV atom M and chalcogenide atom X are shown using green and yellow balls, respectively. The unit cell is indicated by the dashed rectangle in (a). (d) First Brillouin zone of the MX monolayer with high-symmetry points.

$\Gamma - X$ direction, denoted by X^*, and the conduction-band minimum (CBM) locates along the $\Gamma - Y$ direction, indicated by Y^*. However, for the GeSe monolayer it is a direct-band-gap semiconductor, with both VBM and CBM located at X^*. Details of the band gap values and the corresponding positions of VBM and CBM are given in Table I. It is noted that the band gaps of the MX MLs vary over a wide energy range, from 1.01 to 2.74 eV, which is very similar to the Heyd-Scuseria-Ernzerhof (HSE06) hybrid functional predictions (from 1.02 to 2.43 eV) [19].This implies that the band gap of the MX MLs can be tuned by changing the chemical composition. The upper valence bands and the lower conduction bands calculated with DFT-GGA are also shown in Fig. 2. It is interesting to note that the shapes of the bands are insensitive to the choice of exchange-correlation approximations, and the GW approximation increases only the band gap but hardly affects the band dispersion of the MX monolayers.

The electronic transport properties of materials are largely determined by the carrier mobility. As the structural analog

TABLE I. Lattice parameters, a and b, of fully relaxed MX monolayers, structure anisotropy factor κ, defined as $\kappa = (a-b)/(a+b)$, quasiparticle band gaps calculated within the GW approximation, and positions of the VBM and CBM given in units of $2\pi/|a|$ and $2\pi/|b|$ in the x and y directions, respectively. In the parentheses I and D indicate indirect and direct band gap, respectively.

	a (Å)	b (Å)	κ	Band gap (eV)	VBM	CBM
GeS	4.470	3.666	0.099	2.74 (I)	(0.38, 0)	(0, 0.41)
GeSe	4.297	3.968	0.040	1.66 (D)	(0.40, 0)	(0.40, 0)
GeTe	4.400	4.241	0.018	1.21 (I)	(0.38, 0)	(0, 0.41)
SnS	4.290	4.082	0.025	2.24 (I)	(0.39, 0)	(0, 0.41)
SnSe	4.389	4.293	0.011	1.39 (I)	(0.41, 0)	(0, 0.42)
SnTe	4.570	4.559	0.001	1.01 (I)	(0.41, 0)	(0, 0.41)

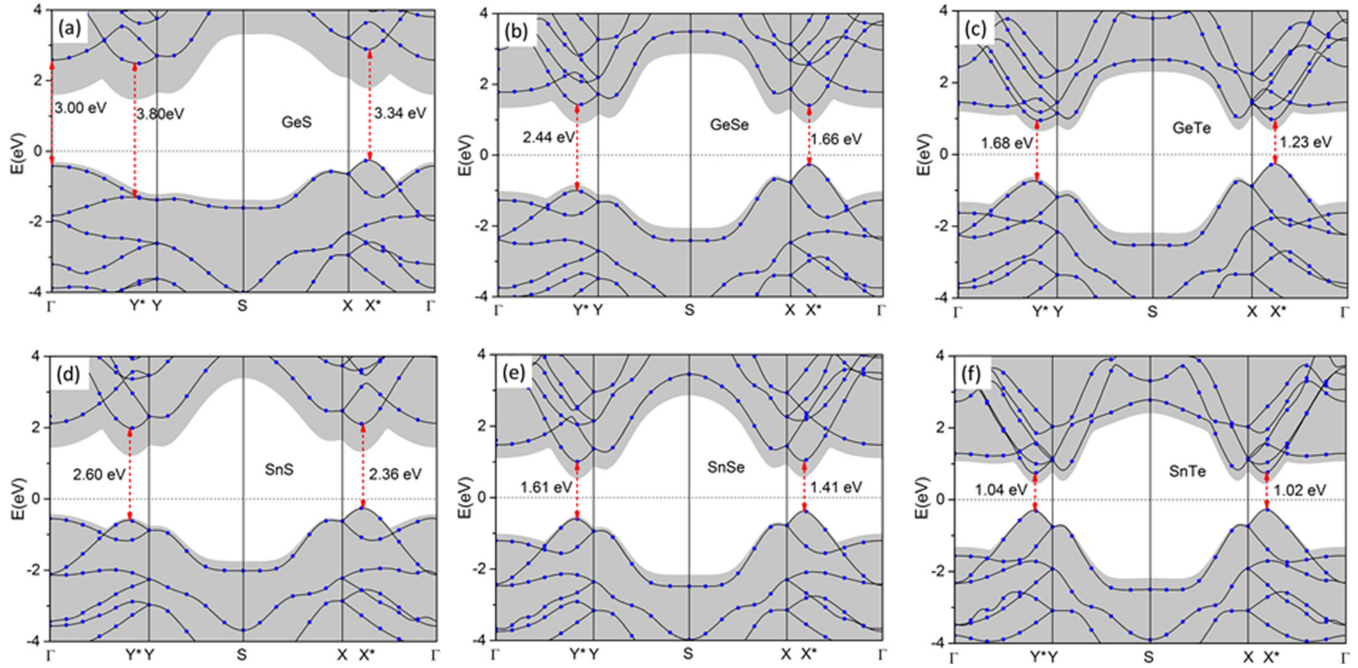

FIG. 2. Quasiparticle band structures of the MX monolayers obtained by Wannier interpolation. The blue solid circles represent the k points that are sampled in GW calculations. The top valance band and bottom conduction band derived from DFT-GGA are shown by shaded gray background. The first excitation transitions along the x and y direction are denoted by the red dashed arrows.

of phosphorene, the MX MLs are expected to possess high carrier mobility. Here, we estimate the carrier mobilities of the MX MLs based on the phonon-limited scattering model, which gives mobility of a 2D system as [29,30]

$$\mu_{2D} = \frac{e\hbar^3 C_{2D}}{k_b T m_e^* m_d \left(E_1^i\right)^2},$$

where m_e^* is the effective mass of the carrier along the transport direction and m_d is the average carrier effective mass, which can be obtained from $m_d = \sqrt{m_x^* m_y^*}$. The term E_1^i represents the deformation potential constant of VBM for holes or CBM for electrons along the transport direction, defined by $E_1^i = \Delta V_i/(\Delta l/l_0)$, where ΔV_i is the energy change of VBM or CBM when the system suffers from a compressive or tensile strain with a magnitude of $\Delta l/l_0$ along the transport direction. The term C denotes the elastic modulus of the longitudinal strain in the propagation direction of the longitudinal acoustic phonons. It can be derived from the equation $(E - E_0)/S_0 = C(\Delta l/l_0)^2/2$, where E is total energy under the corresponding strain and S_0 is the area of the lattice at the equilibrium state. T is the temperature, which is set to 300 K in our calculations. In this work, we vary the strain $\Delta l/l_0$ between −0.5% and 0.5% to fit the parameter E_1^i and from −1% to 1% to fit the parameter C (see the Supplemental Material [31]). It should be noted that the formula we adopted above considers only the interaction between free carriers and longitudinal acoustic phonons. Therefore, the calculated mobility can be regarded only as the intrinsic carrier mobility, which is generally larger than the experiment measured value due to impurity scattering. Since the carrier mobility does not strongly depend on the band gap and PBE functional calculations give a shape of the band structures that agrees with those from GW calculations, for simplicity, we evaluate the carrier mobility at the PBE level of theory, and the relevant parameters are summarized in Table II. Our results for the elastic modulus are in good agreement with results from previous calculations [19,20]. The difference in values in the x and y directions of a given quantity is an indication of the intrinsic in-plane anisotropic mechanical properties. It is noted that the predicted carrier mobilities for MX MLs are high (of the order of 10^3 to 10^5 cm^2 V^{-1} s^{-1}) and highly anisotropic compared with that of monolayer transition-metal dichalcogenides [32]. In contrast to phosphorene [29], the electrons are more mobile than holes in all MX MLs studied here. Furthermore, as shown in Table II, for GeX monolayers, the electron mobility is higher along the x direction, while for SnX monolayers, the electron mobility is higher along the y direction. Finally, we find that the carrier mobility of GeS, GeSe, and SnS monolayers are comparable to that of phosphorene [29], whereas GeTe, SnSe, and SnTe monolayers have much higher mobilities than phosphorene, close to that of monolayer graphene [33]. The exceptionally high carrier mobilities for GeTe, SnSe and SnTe monolayers result from their small effective masses and small deformation potential constants along a particular direction. We want to emphasize that both electron and hole mobilities of the SnTe monolayer are high (2.71×10^5 cm^{-1} V^{-1} s^{-1} for electrons and 1.93×10^4 cm^{-1} V^{-1} s^{-1} for holes), which make it very promising as a semiconductor channel material. We note that the electron mobility of MX monolayers has been calculated with the same method reported here in a recent study [34], and the parameters, like elastic modulus C and effective mass, are consistent with our results. However, their calculated mobility is slightly smaller than our result because the CBM is not aligned using the vacuum level or the core level in their calculations.

TABLE II. Calculated carrier effective mass m^*, deformation potentials constant E, elastic moduli C, and carrier mobility μ.

	Carrier	m_x^* (m_0)	m_y^* (m_0)	E_x (eV)	E_y (eV)	C_x (J m^{-2})	C_y (J m^{-2})	μ_x (cm^{-2} V^{-1} s^{-1})	μ_y (cm^{-2} V^{-1} s^{-1})
GeS	electron	0.22	0.50	0.77	2.46	16.42	44.18	8.08×10^3	0.93×10^3
	hole	0.23	0.92	7.56	4.84	16.42	44.18	0.06×10^3	0.10×10^3
GeSe	electron	0.13	0.40	1.51	6.67	19.75	46.08	6.22×10^3	0.24×10^3
	hole	0.14	0.44	4.60	9.60	19.75	46.08	0.58×10^3	0.10×10^3
GeTe	electron	0.07	0.28	0.52	3.96	14.61	46.04	120.72×10^3	1.59×10^3
	hole	0.12	0.23	3.24	10.05	14.61	46.04	1.47×10^3	0.26×10^3
SnS	electron	0.19	0.20	2.81	3.53	20.96	43.72	1.58×10^3	1.93×10^3
	hole	0.22	0.27	4.06	5.93	20.96	43.72	0.53×10^3	0.42×10^3
SnSe	electron	0.13	0.12	4.24	1.43	32.53	47.15	2.39×10^3	32.08×10^3
	hole	0.12	0.14	3.48	8.12	32.53	47.15	3.62×10^3	0.84×10^3
SnTe	electron	0.09	0.09	6.30	0.66	43.47	43.56	2.96×10^3	270.83×10^3
	hole	0.09	0.05	2.78	9.09	43.47	43.56	19.30×10^3	3.44×10^3

IV. OPTICAL PROPERTIES OF MX MONOLAYERS

It is well known that excitonic effects are remarkable in 2D materials due to weak dielectric screening in such materials [35,36]. Therefore, excitonic effects play an important role in the optical properties and dominate the performance of optoelectronic devices based on 2D materials. It is essential to take the electron-hole Coulomb interaction into consideration when studying optical properties of 2D materials. The GW-BSE approach is known to provide a reliable description of Coulomb interaction between the electron and the hole in an exciton [37]. In this section, we present the results of our investigation on the optical properties of MX MLs using the GW-BSE method. Moreover, in order to have a better idea of the excitonic effects, we also calculate the optical spectra using the GW method within the random-phase approximation (GW-RPA), where the electron-hole interaction is excluded. In Fig. 3, we present the imaginary part of the macroscopic dielectric function, which is directly related to the absorption spectra, for incident light linearly polarized along the x and y directions. As can been seen, the spectrum along the x direction is distinctly different from that along the y direction for all monolayer MXs, and we also note that the spectrum of the SnX monolayer has a smaller degree of anisotropy compared to the GeX monolayer, in particular for the SnTe monolayer, where the absorption spectrum is almost direction independent. When looking at the structure anisotropy factor, which is defined as $\kappa = (a - b)/(a + b)$ in Table I, we can find that the GeX monolayer always shows higher structure anisotropy than the SnX monolayer; for example, the GeS monolayer has the most structure anisotropy, whereas the structure of the SnTe monolayer tends to be isotropic. Thus, we can conclude that the anisotropy of the optical spectrum appearing in the MX monolayer is a consequence of structure anisotropy. In addition, comparing the spectra from GW-RPA and GW-BSE, we find that the optical spectra are completely reshaped when the electron-hole Coulomb interaction is included, which means that the excitonic effects are significant and the optical features are dominated by the excitonic states.

It is noted that the GW-BSE method is limited to direct band excitation, which corresponds to the direct band gap in the quasiparticle band structure. Taking the optical spectrum of the GeS monolayer [shown in Fig. 3(a)] as an example, the transitions concerned are indicated by the red dashed lines in Fig. 2(a), i.e., direct transitions from the highest valance band to the lowest conduction band at Γ, X^*, and Y^*, with band gaps of 3.00, 3.34, and 3.83 eV, respectively. From the band structure, one can easily deduce that the first optical gap (2.23 eV) along the x direction arises from the transition at the Γ point, whereas the first optical gap (3.12 eV) along the y direction originates from the transition at Y^*. The large difference in the first optical gaps along the x direction (2.23 eV) and the y direction (3.12 eV) implies that if the energy of an incident light is between 2.23 and 3.12 eV, only light polarized in the x direction will be absorbed; thus, the GeS monolayer can function as a polarization filter, which has already been realized in experiment for phosphorene [38,39]. Although the energy range of the GeS monolayer is smaller than that of phosphorene (from 1.1 to 2.8 eV) [39–41], it is applicable in a higher working energy region. The exciton binding energy, defined as the difference between the electronic band gap and the optical gap, is a quantitative description of the excitonic effects. Based on the calculated band gap and optical gap, exciton binding energies of 0.77 and 0.71 eV can be derived for excitons at Γ and Y^*, respectively.

As shown in Fig. 2, for the other five MX MLs being studied, the first optical gap along the x direction arises from the direct transition at the X^* point, which is different from GeS, while the first optical gap along the y direction comes from the direct transition at the Y^* point. The calculated quasiparticle gaps, optical gaps, and exciton binding energies for the lowest exciton states along the x and y directions are summarized in Table III. It is seen that the onset energy of optical absorption of the monolayer MXs varies over a broad range (from 0.83 to 2.23 eV), which covers the near-infrared and visible light ranges, which makes monolayer MXs very appealing for photovoltaic and optoelectronic applications. On the other hand, the excitonic effects are significant for all MX MLs, and the exciton binding energy ranges from 0.19 to 0.77 eV, indicating that the excitons are thermally stable at or above room temperature. Furthermore, the exciton binding energy decreases with the atomic number of the group-IV or chalcogen atom, similar to the tendency observed in monolayer TMDs [42]. In order to have a better understanding of the exciton binding energy difference among the MX monolayers, the normalized

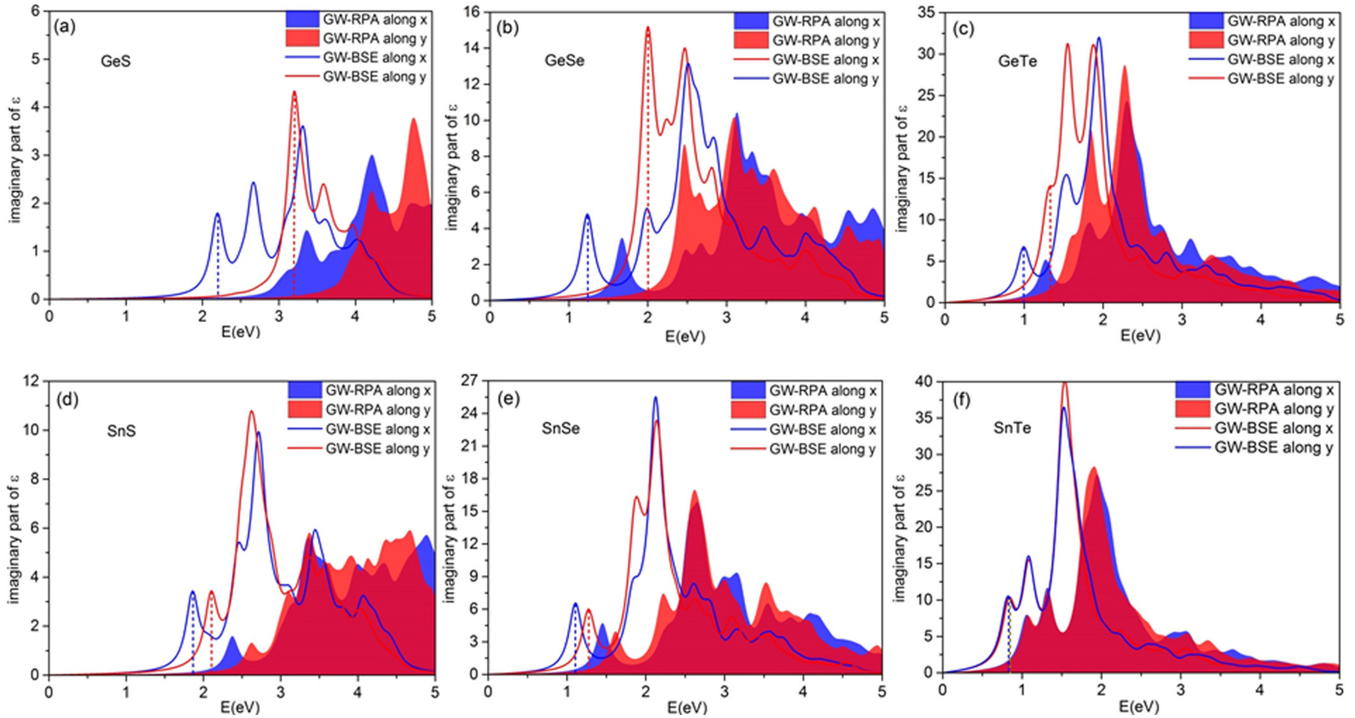

FIG. 3. Optical spectra of the MX monolayers calculated using GW-RPA (without e-h interaction) and GW-BSE (with e-h interaction) methods for linearly polarized light along the x direction and the y direction, respectively. The first optical gaps along the x direction and the y direction are denoted by blue and red vertical dotted lines, respectively.

squared exciton wave functions of GeS and GeTe monolayers are plotted in Figs. 4(a) and 4(c) using the BERKELEYGW code [37], where a 20 × 20 supercell is used and the hole is fixed in the center. It is clear that the exciton is much more localized in the real space for the GeS monolayer, which indicates that the interaction between the electron and hole is very strong, and as a result a large exciton binding energy can be expected.

V. EFFECTIVE-MASS MODEL FOR EXCITONS

As mentioned above, the excitonic effects play a critical role in determining the optical properties of 2D materials, and it is important to have a deep understanding of the exciton feature of MX MLs. However, GW-BSE calculations are very demanding, and it is challenging to study the screening effects with the presence of a dielectric substrate. In this section, we develop a model based on the effective-mass theory. Considering the in-plane anisotropy of the MX MLs, the 2D exciton Hamiltonian can be written as [43]

$$H = -\frac{\hbar^2}{2\mu_x}\frac{\partial^2}{\partial x^2} - \frac{\hbar^2}{2\mu_y}\frac{\partial^2}{\partial y^2} - V_{2D}(x,y), \quad (1)$$

where μ_x and μ_y are the reduced masses of the exciton along the x and y directions, respectively, which can be obtained

TABLE III. Calculated GW gap E_g^{GW}, BSE optical gap E_g^{Opt}, BSE exciton binding energy E_b^{BSE}, 2D polarizability χ_{2D}, reduced exciton mass μ, exciton radius a, and exciton binding energies E_b^M obtained from the effective-mass model for the lowest excitations along the x and y directions for various MX monolayers.

	Direction	E_g^{GW} (eV)	E_g^{Opt} (eV)	E_b^{BSE} (eV)	χ_{2D} (Å)	μ_x,μ_y (Å)	a_x,a_y (Å)	E_b^M (eV)
GeS	x	3.00	2.23	0.77	3.63	0.27, 0.90	6.74, 4.46	0.98
	y	3.83	3.12	0.71	3.63	0.14, 0.31	10.02, 7.56	0.77
GeSe	x	1.66	1.24	0.42	7.26	0.06, 0.16	21.16, 15.41	0.38
	y	2.44	2.00	0.44	7.26	0.06, 0.12	21.73, 17.44	0.36
GeTe	x	1.23	1.00	0.23	14.36	0.05, 0.09	32.77, 27.45	0.21
	y	1.68	1.34	0.34	14.36	0.03, 0.11	40.79, 26.27	0.20
SnS	x	2.36	1.86	0.50	4.85	0.10, 0.10	15.06, 15.06	0.50
	y	2.58	2.10	0.48	4.85	0.09, 0.11	15.91, 14.68	0.50
SnSe	x	1.41	1.11	0.30	8.97	0.05, 0.07	27.34, 25.04	0.28
	y	1.61	1.28	0.33	8.97	0.05, 0.06	27.09, 25.83	0.28
SnTe	x	1.02	0.83	0.19	19.31	0.03, 0.04	52.22, 45.21	0.14
	y	1.04	0.85	0.19	19.31	0.03, 0.04	52.22, 45.21	0.14

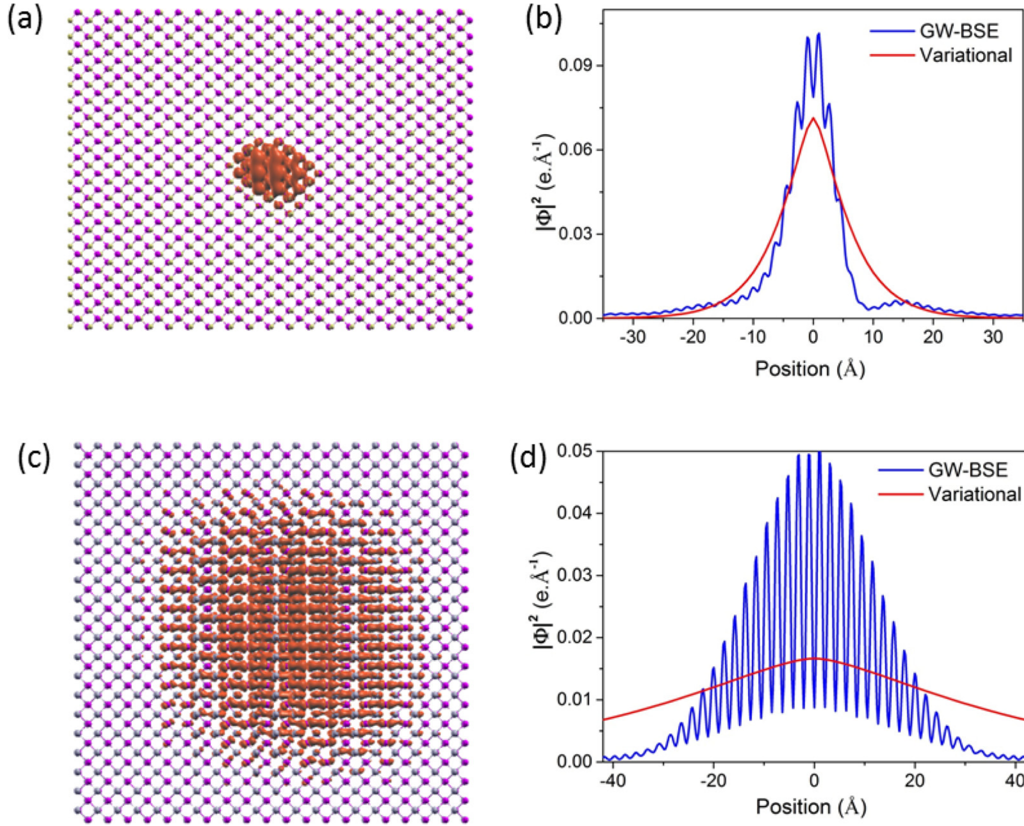

FIG. 4. Normalized squared exciton wave function calculated using GW-BSE for (a) the GeS monolayer and (c) the GeTe monolayer. The isovalue is set to $3 \times 10^{-6}\, e\, \text{Å}^{-3}$, and the hole is fixed at the center. Comparison of the exciton wave-function distribution along the zigzag direction between GW-BSE and variational methods for (b) the GeS monolayer and (d) the GeTe monolayer.

from $\mu_i^{-1} = (m_i^e)^{-1} + (m_i^h)^{-1}$, $i = x,y$, and $V_{2D}(x,y)$ is the Coulomb potential due to a point charge located at the origin in the 2D dielectric space. According to Keldysh [44], this potential has the following form:

$$V_{2D}(r) = \frac{e^2}{4\varepsilon_0(\varepsilon_1+\varepsilon_2)r_0}\left[H_0\left(\frac{r}{r_0}\right) - Y_0\left(\frac{r}{r_0}\right)\right], \quad (2)$$

where H_0 and Y_0 are the zeroth-order Struve function and the zeroth-order Bessel function of the second kind, r_0 is the screening length, and ε_1 and ε_2 are the dielectric constants of the media above and below the MX monolayer, respectively. At a large separation between the electron and the hole, the potential approaches the screened Coulomb potential r^{-1}, while at short electron-hole separation, it diverges logarithmically. The critical separation is determined by the screening length r_0. Recently, Cudazzo *et al.* [45] proposed the following approximation to the Keldysh Coulomb potential:

$$V_{2D}(r) = \frac{e^2}{2\pi\varepsilon_0(\varepsilon_1+\varepsilon_2)r_0} \times \left[\ln\left(\frac{r}{r+r_0}\right) + [\gamma - \ln(2)]e^{-\frac{r}{r_0}}\right], \quad (3)$$

where γ is the Euler constant. It has been shown that this approximation is in excellent agreement with the Keldysh potential in both limits [43]. However, compared to the original Keldysh form, this approximation is simpler to implement, and it is adopted in our numerical calculations.

The reduced exciton mass can be directly obtained from first-principles GW calculations, and values are listed in Table III. Another key parameter is the screening length r_0, which depends on the polarizability χ of the 2D material as $r_0 = 4\pi\chi/(\varepsilon_1+\varepsilon_2)$ [45]. The polarizability χ of a 2D material can be derived from [45]

$$\varepsilon(L) = 1 + \frac{4\pi\chi}{L}, \quad (4)$$

where $\varepsilon(L)$ is the in-plane dielectric constant of the corresponding three-dimensional layered structure with interlayer separation L. In the present study, ε is computed at different interlayer distances L at the level of GW-RPA theory, and χ is obtained with a linear fitting of the $\varepsilon(L)$-L^{-1} curve. As an example, we show in Fig. 5(a) the calculated in-plane dielectric constants, ε_x and ε_y, as functions of inverse interlayer separation L for bulk GeS. From the linear fitting, we obtain $\chi_x = 3.67$ Å and $\chi_y = 3.59$ Å. Since these two values are very close to each other, for simplicity, the average value of $\chi = 3.63$ Å is used, which results in a screening length of $r_0 = 22.81$ Å for monolayer GeS. The same treatments were done for other MX MLs, and the resulting 2D polarizabilities are listed in Table III. We note that the polarizability tends to increase with the chalcogen atom and the SnX monolayer always has a larger polarizability than the GeX monolayer; in

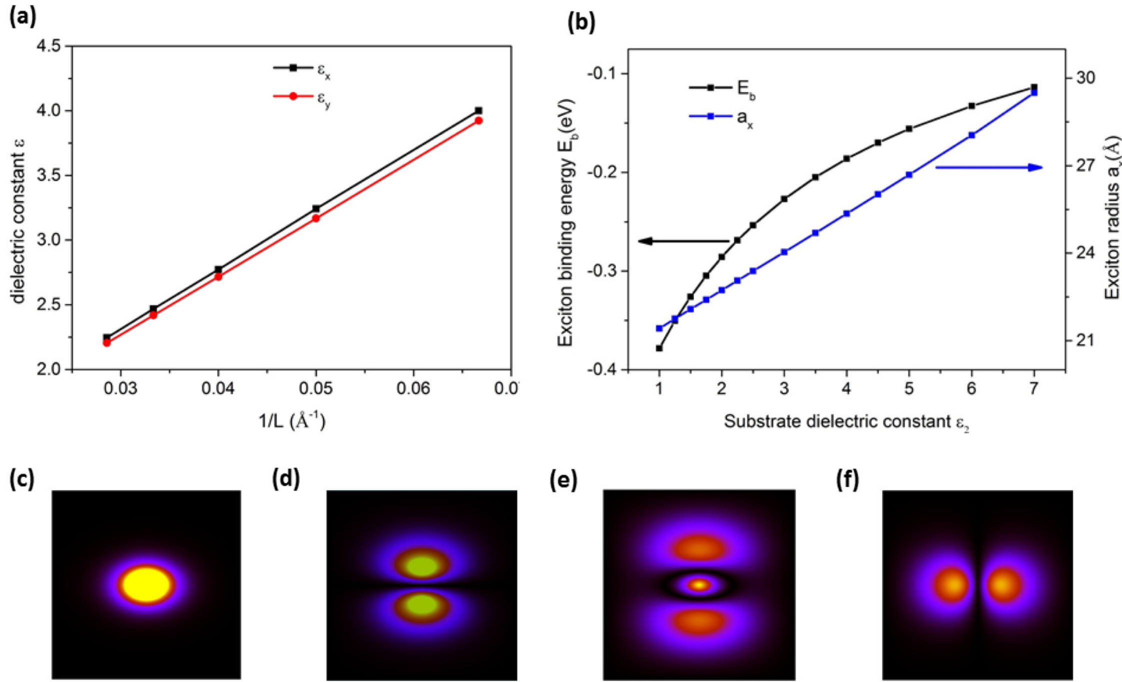

FIG. 5. (a) In-plane dielectric constants, ε_x and ε_y, as functions of inverse interlayer separation $1/L$ for the GeS monolayer. (b) Exciton binding energy E_b and radius a_x as a function of substrate dielectric constant ε_2 for the GeSe monolayer. (c)–(f) Squared wave functions $|\psi_n|^2$ for the four lowest energy exciton states of GeSe monolayer, shown in 200 Å × 200 Å.

fact, the polarizability can be regarded as the material intrinsic screening strength. Therefore, the difference in the polarizabilities among the MX monolayers will give a different screening to the e-h interaction and result in a different exciton binding energy.

The variational method is used to determine the exciton ground-state energy, with the following trial wave function:

$$\Phi(\mathrm{x,y}) = \left(\frac{2}{\pi a_x a_y}\right)^{1/2} \exp\left\{-\left[\left(\frac{x}{a_x}\right)^2 + \left(\frac{y}{a_y}\right)^2\right]^{1/2}\right\}, \tag{5}$$

where a_x and a_y are the exciton radii along the x direction and the y direction, respectively, which are treated as variational parameters. The Schrödinger equation is solved numerically, and the lowest eigenvalue of the Hamiltonian gives the exciton binding energy. In Table III, we summarize the numerical results for the exciton binding energies and their radii along the x and y directions for various MX MLs considered. By comparing the calculated exciton binding energies with those obtained using the BSE calculation, we find that they correlate very well. The largest deviations occur for GeS in the x direction (0.21 eV) and GeTe in the y direction (−0.14 eV). All other values are within 0.06 eV of the BSE results. This means that the simple effective-mass model gives a good description of the exciton property. It is also noted that the exciton radii are generally smaller than the screening length r_0 $(2\pi\chi)$, which reveals that the 2D Coulomb potential behaves close to the logarithmic limit, and treating the 2D potential as a screened $1/r$ Coulomb potential, as done in Ref. [46] for GeS and SnS, is inappropriate. The exciton radii of GeSe and SnSe obtained in the present study are also in good agreement with the values (17 and 20 Å) of first-principles calculations reported in Ref. [16]. In Figs. 4(b) and 4(d), we compare distributions of the squared exciton wave function along the zigzag direction between GW-BSE and variational results for GeS and GeTe monolayers, respectively. We can see that the agreement is very good for the GeS monolayer, while for the GeTe monolayer the agreement is somewhat poor, which may be due to the fact that variational method is not good at giving a precise wave function. Regardless, they both show that the exciton in the GeS monolayer is much more localized than that in the GeTe monolayer. Based on the predicted exciton radius, as shown in Table III, we can conclude that when the exciton is more delocalized, its exciton binding energy will become smaller. Interestingly, the exciton binding energy weakly depends on the reduced mass but is very sensitive to screening length, which means that the potential $V_{2D}(x,y)$ in Eq. (1) dominates the exciton binding energy. Based on this fact, we can deduce that an indirect exciton would have binding energy similar to that of the direct exciton even though the recombination process for the indirect exciton is more complex due to the involvement of phonon-assisted scattering.

For many applications that require separation of electrons and holes such as in optoelectronic devices, the large exciton binding energy is undesirable since it prevents the exciton dissociation process and accelerates the e-h recombination process. An efficient way to reduce the exciton binding energy is to use a substrate, which can provide a dielectric screening to the electron-hole Coulomb interaction [47]. Here, the effective mass model is used to investigate how the dielectric substrate affects the exciton behavior. We set ε_1 to 1 to mimic the vacuum environment on top of the MX monolayer and vary

the value of ε_2 to simulate the effect of different substrates at the bottom of the MX monolayer. Due to the importance of a direct gap in photonic applications, we focus the discussion below on the monolayer GeSe. The calculated exciton binding energy and radius a_x are shown in Fig. 5(b) as functions of the dielectric constant of the substrate. The exciton binding energy decreases very quickly with increasing dielectric constant. For example, the exciton binding energy is reduced from 0.38 eV for suspended GeSe to 0.19 eV when GeSe is supported on a SiO_2 substrate (3.9) [48]. With the decrease of the exciton binding energy, the exciton state becomes more delocalized, which is reflected in the nearly linear increase of the exciton radius with the dielectric constant of the substrate. Our work confirms that the dielectric substrate is an effective way of reducing the exciton binding energy and thus improving the performance of optoelectronic and solar cell devices.

Finally, we would like to point out that it is possible to obtain some excited states by direct diagonalization of the effective-mass Hamiltonian (1) using the Lanczos method. The energies of the four lowest exciton states obtained using this method are −0.38, −0.21, −0.16, and −0.10 eV, respectively. The corresponding wave functions are shown in Figs. 5(c)–5(f). Obviously, the orbitals show $1s$, $2p_y$, $2s$, and $2p_x$ characters. Since an exciton with finite orbital angular momentum is dipole forbidden and does not contribute to the linear absorption spectrum, only the $1s$ and $2s$ states in the absorption spectrum can be detected, like for other 2D materials [49,50] where several bound s states have been observed. The exciton oscillator strength is proportional to $|\psi_n(0,0)|^2$ [51]. In our calculations, the squared modulus of the exciton wave function for the $1s$ state is about 6 times larger than that of the $2s$ state. This indicates that the first peak, which originates from the $1s$ state, should have much higher intensity in the absorption spectrum than the second peak, which results from the $2s$ state.

VI. CONCLUSIONS

In summary, we have systematically investigated the electronic and optical properties of a class of monolayer group-IV MX monochalcogenides using first-principles calculations. All MX MLs show semiconducting character with band gap ranging from 1.01 to 2.74 eV. In particular, the GeSe monolayer has a direct band gap, while all others have indirect band gaps. All MX MLs are predicted to possess high carrier mobilities and can be potential channel materials in electronic devices. In addition, the onset optical absorption energies of MX MLs cover a broad and technologically important range from near infrared to visible, which make them very appealing for optoelectronic and photovoltaic applications. More importantly, the exciton binding energies obtained from the effective-mass model are in good agreement with that obtained from GW-BSE calculations. Using this model, we have investigated the substrate effect on the exciton properties of the GeSe monolayer. It is found that the exciton binding energy decreases quickly with increasing dielectric constant of the substrate, while the exciton radius increases almost linearly with the dielectric constant of the substrate. Our results provide useful guidance for experiment optimization of the excitonic effects by substrate engineering.

ACKNOWLEDGMENTS

The authors acknowledge financial support from a Singapore Ministry of Education Academic Research grant (Grant No. WBS R144000361112). M.Y. and S.J.W. are grateful for the funding support from the Singapore A*STAR 2D PHAROS project: 2D devices & materials for ubiquitous electronic, sensor and optoelectronic applications (Project No. SERC 1527000012). We also acknowledge computational resources provided by the Centre for Advanced 2D Materials (CA2DM) at the National University of Singapore.

[1] K. S. Novoselov, A. K. Geim, S. V. Morozov, D. Jiang, M. I. Katsnelson, I. V. Grigorieva, S. V. Dubonos, and A. A. Firsov, Nature (London) **438**, 197 (2005).
[2] L. Song *et al.*, Nano Lett. **10**, 3209 (2010).
[3] K. F. Mak, C. Lee, J. Hone, J. Shan, and T. F. Heinz, Phys. Rev. Lett. **105**, 136805 (2010).
[4] L. Li, Y. Yu, G. J. Ye, Q. Ge, X. Ou, H. Wu, D. Feng, X. H. Chen, and Y. Zhang, Nat. Nanotechnol. **9**, 372 (2014).
[5] G. Eda, H. Yamaguchi, D. Voiry, T. Fujita, M. Chen, and M. Chhowalla, Nano Lett. **11**, 5111 (2011).
[6] K. S. Novoselov, A. K. Geim, S. V. Morozov, D. Jiang, Y. Zhang, S. V. Dubonos, I. V. Grigorieva, and A. A. Firsov, Science **306**, 666 (2004).
[7] B. Radisavljevic, A. Radenovic, J. Brivio, V. Giacometti, and A. Kis, Nat. Nanotechnol. **6**, 147 (2011).
[8] W. Han, R. K. Kawakami, M. Gmitra, and J. Fabian, Nat. Nanotechnol. **9**, 794 (2014).
[9] L. C. Gomes, A. Carvalho, and A. H. Castro Neto, Phys. Rev. B **92**, 214103 (2015).
[10] P. D. Antunez, J. J. Buckley, and R. L. Brutchey, Nanoscale **3**, 2399 (2011).
[11] L. D. Zhao, S. H. Lo, Y. Zhang, H. Sun, G. Tan, C. Uher, C. Wolverton, V. P. Dravid, and M. G. Kanatzidis, Nature (London) **508**, 373 (2014).
[12] M. Xu, T. Liang, M. Shi, and H. Chen, Chem. Rev. **113**, 3766 (2013).
[13] P. Sinsermsuksakul, J. Heo, W. Noh, A. S. Hock, and R. G. Gordon, Adv. Energy Mater. **1**, 1116 (2011).
[14] A. K. Singh and R. G. Hennig, Appl. Phys. Lett. **105**, 042103 (2014).
[15] D. J. Xue, J. Tan, J. S. Hu, W. Hu, Y. G. Guo, and L. J. Wan, Adv. Mater. **24**, 4528 (2012).
[16] G. Shi and E. Kioupakis, Nano Lett. **15**, 6926 (2015).
[17] M. Wu and X. C. Zeng, Nano Lett. **16**, 3236 (2016).
[18] L. C. Gomes, A. Carvalho, and A. H. Castro Neto, Phys. Rev. B **94**, 054103 (2016).
[19] L. Huang, F. Wu, and J. Li, J. Chem. Phys. **144**, 114708 (2016).
[20] R. Fei, W. Li, J. Li, and L. Yang, Appl. Phys. Lett. **107**, 173104 (2015).
[21] A. S. Rodin, L. C. Gomes, A. Carvalho, and A. H. Castro Neto, Phys. Rev. B **93**, 045431 (2016).

[22] G. Kresse and J. Furthmüller, Phys. Rev. B **54**, 11169 (1996).
[23] J. P. Perdew, K. Burke, and M. Ernzerhof, Phys. Rev. Lett. **77**, 3865 (1996).
[24] P. E. Blöchl, Phys. Rev. B **50**, 17953 (1994).
[25] H. J. Monkhorst and J. D. Pack, Phys. Rev. B **13**, 5188 (1976).
[26] N. Marzari, A. A. Mostofi, J. R. Yates, I. Souza, and D. Vanderbilt, Rev. Mod. Phys. **84**, 1419 (2012).
[27] A. A. Mostofi, J. R. Yates, G. Pizzi, Y.-S. Lee, I. Souza, D. Vanderbilt, and N. Marzari, Comput. Phys. Commun. **185**, 2309 (2014).
[28] J. Paier, M. Marsman, and G. Kresse, Phys. Rev. B **78**, 121201 (2008).
[29] J. Qiao, X. Kong, Z. X. Hu, F. Yang, and W. Ji, Nat. Commun. **5**, 4475 (2014).
[30] S. Takagi, A. Toriumi, M. Iwase, and H. Tango, IEEE Trans. Electron Devices **41**, 2357 (1994).
[31] See Supplemental Material at http://link.aps.org/supplemental/10.1103/PhysRevB.95.235434 for calculation details of the deformation potential constant E and elastic modulus C.
[32] Y. Cai, G. Zhang, and Y.-W. Zhang, J. Am. Chem. Soc. **136**, 6269 (2014).
[33] E. H. Hwang and S. Das Sarma, Phys. Rev. B **77**, 115449 (2008).
[34] A. Shafique and Y.-H. Shin, Sci. Rep. **7**, 506 (2017).
[35] D. Y. Qiu, F. H. da Jornada, and S. G. Louie, Phys. Rev. Lett. **111**, 216805 (2013).
[36] J. H. Choi, P. Cui, H. Lan, and Z. Zhang, Phys. Rev. Lett. **115**, 066403 (2015).
[37] M. Rohlfing and S. G. Louie, Phys. Rev. B **62**, 4927 (2000).
[38] X. Wang *et al.*, Nat. Nanotechnol. **10**, 517 (2015).
[39] L. Li *et al.*, Nat. Nanotechnol. **12**, 21 (2017).
[40] C. E. Villegas, A. S. Rodin, A. Carvalho, and A. R. Rocha, Phys. Chem. Chem. Phys. **18**, 27829 (2016).
[41] V. Tran, R. Soklaski, Y. Liang, and L. Yang, Phys. Rev. B **89**, 235319 (2014).
[42] A. Ramasubramaniam, Phys. Rev. B **86**, 115409 (2012).
[43] E. Prada, J. V. Alvarez, K. L. Narasimha-Acharya, F. J. Bailen, and J. J. Palacios, Phys. Rev. B **91**, 245421 (2015).
[44] L. V. Keldysh, JETP Lett. **29**, 658 (1979).
[45] P. Cudazzo, I. V. Tokatly, and A. Rubio, Phys. Rev. B **84**, 085406 (2011).
[46] B. R. Tuttle, S. M. Alhassan, and S. T. Pantelides, Phys. Rev. B **92**, 235405 (2015).
[47] M. M. Ugeda *et al.*, Nat. Mater. **13**, 1091 (2014).
[48] P. R. Gray and R. G. Meyer, *Analysis and Design of Analog Integrated Circuits* (Wiley, New York, 1990).
[49] A. Chernikov, T. C. Berkelbach, H. M. Hill, A. Rigosi, Y. Li, O. B. Aslan, D. R. Reichman, M. S. Hybertsen, and T. F. Heinz, Phys. Rev. Lett. **113**, 076802 (2014).
[50] A. Chaves, T. Low, P. Avouris, D. Çakır, and F. M. Peeters, Phys. Rev. B **91**, 155311 (2015).
[51] R. J. Elliott, Phys. Rev. **108**, 1384 (1957).